

Single-Chain Properties of Polyelectrolytes in Poor Solvent[†]

Hans Jörg Limbach* and Christian Holm

Max-Planck-Institut für Polymerforschung, Ackermannweg 10, 55128 Mainz, Germany

Received: December 3, 2002; In Final Form: June 2, 2003

Using molecular dynamics simulations in which we take counterions explicitly into account, we study the behavior of a dilute solution of strongly charged polyelectrolytes in poor solvents. We focus on the chain conformational properties under conditions in which chain–chain interactions can be neglected but the counterion concentration remains finite. We investigate the conformations with regard to the parameters chain length, Coulomb interaction strength, and solvent quality and explore in which regime the competition between short-range hydrophobic interactions and long-range Coulomb interactions leads to pearl-necklace-like structures. We observe that large number and size fluctuations in the pearls and strings lead to only small direct signatures in experimental observables like the single-chain form factor. Furthermore, we do not observe the predicted first-order collapse of the necklace into a globular structure when counterion condensation sets in. We will also show that the pearl-necklace regime is rather small for strongly charged polyelectrolytes at finite densities. Even small changes in the charge fraction of the chain can have a large impact on the conformation due to the delicate interplay between counterion distribution and chain conformation.

1. Introduction

Polyelectrolytes (PEs) are polymers that have the ability to dissociate charges in polar solvents resulting in charged polymer chains (macroions) and small mobile counterions.¹ Because of their great relevance in technical applications, as well as in molecular biology, they enjoy increasing attention in the scientific community.^{2–5} The combination of macromolecular properties and long-range electrostatic interactions results in an impressive variety of phenomena, which makes these systems interesting from a fundamental point of view.

In this paper, we focus on the special case of polyelectrolytes under poor-solvent conditions. The reason for this is that a large number of polymers are based on a hydrocarbon backbone for which water is a very poor solvent. The solubility in water is often only given because of their charged side groups. Important examples are sulfonated polystyrene (PSS), poly(methacrylic acid) (PMA), DNA, and virtually all proteins. The poor-solvent conditions give rise to a competition between the attractive interactions due to the poor solubility of the backbone and the electrostatic repulsion of the PE charges. This can lead to elongated strings of locally collapsed structures (pearls), commonly called pearl necklaces. Such necklace conformations have been proposed on the basis of fluorescence studies.⁶ They have also been predicted in terms of scaling arguments in refs 7–9 for a weakly charged single chain PE. Later this has been extended to strongly charged chains and finite concentrations.^{10–13} Also other theoretical approaches support the existence of necklace conformations.^{14–16} The scaling approach of ref 9 was supplemented with a Monte Carlo simulation of a single chain that shows a cascade from one to two to three globules with increasing strength of the electrostatic repulsion. In their study, the polyelectrolyte was weakly charged and every monomer carried a fractional charge. The chain was studied in the infinite dilution limit, where counterions do not have to be taken into account. The formation of the necklace structure is due to the

Rayleigh instability of a charged droplet, which leads to a split once a critical charge is reached. The size of the pearls is determined by the balance between electrostatic repulsion and surface tension. The distance between two pearls is governed by the balance of the electrostatic pearl–pearl repulsion and the surface tension.

Some aspects of the theoretical pearl-necklace picture have been confirmed by simulations using the Debye–Hückel approximation^{17,18} and simulations using the full Coulomb interaction and explicit counterions.^{19–24} However, there is, up to now, no clear experimental proof for the existence of necklace chains. Conformational chain properties have been observed that seem to be consistent with the necklace picture.^{6,25–30}

Also the scaling of the peak position of the structure factor q^* with the polymer density ρ has been thoroughly investigated, which however reveals only properties that occur in the semidilute regime of interacting chains. For good solvent chains in the semidilute regime, the exponent β in the scaling relation $q^* \propto \rho^\beta$ was measured to be $\beta = 0.5$, which is also the theoretically predicted value,³¹ whereas for poor-solvent polyelectrolytes, no single value for the exponent seems to exist. The experimental values vary between $\beta = 0.3$ and $\beta = 0.5$ ^{32–35} and show a dependence on the charge fraction of monomers, which is implicitly also responsible for the poor-solvent parameter of the chain. The theoretical predictions show (for fixed poor solvent and fixed charge fraction) also a complicated transition from a $\beta = 1/2$ regime via a $\beta = 1/3$ into a crossover scaling,^{12,13} whereas recent simulations measured a constant exponent $\beta = 1/3$ for the whole concentration range from semidilute up into the dense regime,²⁴ so its fair to say that things are far from being well understood.

However, even for the dilute concentration regime, the situation can be more complicated as envisioned in the scaling approach, because the entropy of the chain and of the counterions, as well as the electrostatic interaction between counterions and the PE charges, have to be taken into account. In our previous shorter communications, we reported large conforma-

[†] Part of the special issue "International Symposium on Polyelectrolytes".

tional fluctuations^{22–24} in the pearl-necklace structures and showed that they were responsible for the absence of strong signatures in the force extension relation and in the form factor.

The aim of the present simulational study is a more detailed investigation of the structure of strongly charged polyelectrolytes in poor solvent in the dilute concentration regime, in which the chain–chain interaction is weak so one deals effectively with single-chain properties. Our focus will be a thorough data analysis of the observed pearl-necklace conformations. To this end, we had to develop a new cluster-recognition algorithm that is capable of characterizing these interesting conformations automatically from our simulated configurational data. Moreover, we look at the stability of the pearl-necklace conformations in the presence of condensed counterions and perform a study of the Coulomb-induced collapse transition. We will compare our results with predictions from scaling theory and will discuss the validity range of the scaling approach for strongly charged chains at finite density. We then attempt to give a preliminary phase diagram for the systems studied. The last part will be devoted to some experimentally accessible observables, such as characteristic chain size ratios and form factor. This should be helpful in supporting the evaluation of experimental data in terms of pearl-necklace signatures.

Our paper is organized as follows: After explaining the used simulation method in section 2 and giving a short overview over the simulated systems in section 3, we will discuss our data analysis methods in section 4. In section 5, we will compare our results in the pearl-necklace regime with predictions made by scaling theories. In section 6, we will quantify the role of fluctuations, and we describe in section 7 our view of the Coulomb-induced collapse transition and a preliminary phase diagram for the range of our simulation parameters. We then discuss in detail some measurable observables in section 8 and finally end with our conclusion in section 9. In the appendix, we give a detailed overview of the simulated systems, including a list of parameters and results for selected basic observables.

2. Simulation Method

Our model of a PE solution and our molecular dynamics approach has been described previously in detail in refs 19, 22, and 36. It consists of N_p flexible bead-spring chains with N_m monomers and N_c counterions, which are located in a cubic simulation box of length L with periodic boundary conditions. A fraction f of the monomers is monovalently charged ($\nu_m = 1$). Thus the total charge per chain is $Q_p = fN_m$. The number of counterions, which are also monovalently charged ($\nu_c = -1$) is chosen such that the overall system is electrically neutral. Densities are given either as monomer density $\rho_m = N_p N_m / L^3$ or as charge density $\rho_c = 2fN_p N_m / L^3$.

All particles interact via a Lennard-Jones (LJ) potential, $4\epsilon - [(\sigma/r)^{12} - (\sigma/r)^6 - c]$ for distances $r < R_c$ and zero elsewhere. The constant c is chosen such that the potential value is zero at the cutoff R_c , and ϵ is a measure of the solvent quality. Monomers interact up to $R_c = 2.5\sigma$ giving them a short-range attraction, which can be tuned by changing the value of ϵ . The counterions interact via a purely repulsive LJ interaction with $R_c = 2^{1/6}\sigma$. Single units of length, energy, and time are denoted by σ , ϵ , and τ , respectively.

The chain monomers are, in addition, connected along the chain by the finite extendible nonlinear elastic (FENE) bond potential of the form $-14k_B T \ln[1 - (r/(2\sigma))^2]$, which results in an average bond length $b \approx 1.1\sigma$.

Charged particles with charges q_i and q_j at separation r_{ij} interact via the Coulomb energy, $k_B T \epsilon_0 q_i q_j / r_{ij}$, where the Bjerrum

length is defined as $\ell_B = e^2 / (4\pi\epsilon_0 k_B T)$ (e = unit charge; ϵ_0 and ϵ_S = permittivity of the vacuum and of the solvent). The Coulomb interaction was calculated with the P3M-algorithm^{37,38} tuned to force accuracies, which are much higher than the thermal noise level.

A velocity Verlet algorithm with a standard Langevin thermostat is used to integrate the equation of motion³⁹ (friction coefficient $\Gamma = \tau^{-1}$; time step $\Delta t = 0.0125\tau$). Thus, the solvent is only implicitly present via its permittivity ϵ_S , the friction constant Γ , and the solvent quality parameter ϵ in the LJ potential.

The simulation time after equilibration for all systems was at least 100 times the measured correlation time for the end-to-end distance R_E and the centers of mass of the chains diffused at least several radii of gyration R_G . The osmotic pressure p was measured to be always positive, and additional simulations over a large density range²⁴ showed that the pV diagram is convex at all densities; thus, our simulations are stable, reach true thermal equilibrium, and reside in a one-phase region. The volume density inside the pearls does not exceed 0.47, which is below the glass transition. We therefore are certain that also the pearl formation and restructuring was observed in equilibrium.

3. Simulated Systems

We have simulated our poor-solvent polyelectrolytes mainly as a function of the parameters chain length N_m , solvent quality ϵ , strength of the electrostatic interaction ℓ_B , and charge fraction f . All simulations are performed in dilute solution such that the interaction between the chains is small. For the system with the longest chains ($N_m = 478$), we have a chain extension $R_E \approx 60\sigma$ and a chain-chain separation $r_{cc} \approx 252\sigma$, which was calculated for a random packing of spheres according to

$$r_{cc} \approx 1.28 \left(\frac{3\pi}{4} \frac{L^3}{N_p} \right)^{1/3} \quad (1)$$

The screened renormalized monopole interaction, U_{cc}^{DH} , between two chains can be estimated for this case to be of the order $k_B T$. For our estimate, we have used a crude approximation on the Debye–Hückel level. The effective chain charge, $Q_{p,eff} \approx 64$, is calculated by using the counterions within a shell of 3σ around the polyelectrolyte to renormalize the bare charge, $Q_p = 160$. The density of the free counterions, $\tilde{\rho}_c$, leads to a screening constant, $\kappa = \sqrt{4\pi\tilde{\rho}_c} \approx 0.009\sigma^{-1}$, and as the interaction potential, we take $U_{cc}^{DH} = \ell_B Q_{p,eff}^2 e^{-\kappa r_{cc}} r_{cc}^{-1} \approx 2.3k_B T$. For this estimate, one has to keep in mind that both the used practical definition of the effective charge, as well as the screening concept, cannot be founded on physical principles.

Details about the used parameters and measurements of some basic observables for all simulated systems can be found in Appendix A. We have grouped the simulations into series depending on the investigated parameters.

The chain-length dependence is studied in simulation series that differ in the line charge density f . For series A1, we use a charge fraction $f = 1/3$, and the chain length is varied over one decade in steps of 48 from $N_m = 48$ to 478. Series A2 and A3 are performed at $N_m = 100, 200$, and 300 with $f = 1/2$ at slightly different densities.

To study the dependence on the solvent quality, we have varied the short-range attraction by changing the LJ parameter ϵ between $0.0k_B T$ and $2.0k_B T$ for medium-sized chains of length $N_m = 238$ (series B). The Θ -point for this model was determined to be at $\epsilon(\Theta) = 0.34k_B T$.¹⁹ For most of the other simulations

(series A1, A2, A3, C1, C2, and C3), we used $\epsilon = 1.75k_B T$, which is thus deep in the poor-solvent regime. This value is chosen for practical reason. In this regime, we have found relatively large and stable pearl-necklace conformations, which are easier to investigate.

The effect of the Coulomb interaction is studied via changing the Bjerrum length ℓ_B and the charge fraction f . We simulated chains with length $N_m = 199$ in three series, C1, C2, and C3, with charge fractions $f = 1$, $f = 1/2$, and $f = 1/3$, respectively. They are performed at the same charge density, $\rho_c = (5 \times 10^{-5})\sigma^{-3}$, but they contain different numbers of counterions, $N_c = fN_m N_P$, corresponding to the number of charges on the PEs. All three series start out at $\ell_B = 0\sigma$. In series C1, ℓ_B ranges up to 10σ and in series C2 and C3 up to 9σ . In addition, there is a simulation set with shorter chains, $N_m = 94$, with $f = 1/3$ and a different solvent parameter $\epsilon = 1.5k_B T$, which we only use for the phase diagram (series C4).

The last series contains four simulations with the same value for the scaling variable, $\ell_B b^{-1} f^2 = 0.25$, but different $f = 1$, $1/2$, $1/3$, and $1/4$ (series D).

4. Observables and Data Analysis

In this section, we define our measured observables and explain in detail how we analyzed our simulated PE conformations. Especially, we present the cluster-recognition algorithm that we used to automatically classify different pearl-necklace structures.

We denote the position of monomer i with \mathbf{r}_i and the distance between two particles i and j with r_{ij} . The center of mass for the chain is then $\mathbf{R}_s = (1/N_m) \sum_{i=1}^{N_m} \mathbf{r}_i$, and the center of mass coordinates are $\mathbf{x}_i = \mathbf{r}_i - \mathbf{R}_s$. For the chain extension, we use the end-to-end distance

$$R_E^2 = (\mathbf{r}_1 - \mathbf{r}_{N_m})^2 \quad (2)$$

the radius of gyration

$$R_G^2 = \frac{1}{N_m} \sum_{i=1}^{N_m} |\mathbf{x}_i|^2 \quad (3)$$

and the inverse hydrodynamic radius

$$R_H^{-1} = \frac{1}{N_m(N_m - 1)} \sum_{i \neq j} \frac{1}{r_{ij}} \quad (4)$$

Note that this definition corresponds to the short-time diffusion behavior of polymers. For more information on this topic, see ref 40. For a first structure classification, we use two characteristic ratios between the different chain extension observables. The first characteristic ratio is defined as $r = (R_E/R_G)^2$. The second characteristic ratio is $\alpha = R_G/R_H$, which has the advantage of being experimentally accessible.⁴¹

We will also compute the spherically averaged form factor, sometimes also called single-chain structure factor, $S_1(q)$, which can be measured in scattering experiments:

$$S_1(q) = \frac{1}{N_m} \sum_{i=1}^{N_m} \sum_{j=1}^{N_m} \frac{\sin(qr_{ij})}{qr_{ij}} \quad (5)$$

To describe the counterion distribution around polyelectrolytes, we use an integrated counterion distribution, $P(r)$. The distance d_i of a counterion i from a chain is defined as the distance of

the counterion from its closest monomer in space. We denote the set of counterions belonging to one chain with \mathcal{C} . From this, we can calculate $P(r)$ as

$$P(r) = \frac{1}{Q_P} \int_{r'=0}^r dr' \sum_{i \in \mathcal{C}} \delta(r' - d_i) \quad (6)$$

$P(r)$ denotes the fraction of counterions that are inside a shell with radius r around a polyelectrolyte chain. This definition can be used for a large variety of chain conformations.

For an automated analysis of all types of pearl-necklace structures appearing in our configurational data, we need a tool to determine to which pearl or string each monomer belongs and what is the total number of such substructures. First, we should state that there is no sharp definition of a pearl or a string. So what we need is a practical approach to the problem. Our guideline in the development of an automated tool for the identification of pearls and strings is that the result should be close to the result that would be obtained by looking at the conformation by eye.

Before we give a detailed explanation of the used cluster-recognition algorithm, we want to present some other methods that are based on observables that could be accessible with experimental methods. In this way, one can also judge how easily these structures can be observed by current experimental techniques.

The local monomer concentration, $\rho_m(\mathbf{r})$, of a chain is given by $\rho_m(\mathbf{r}) = \sum_i \delta(\mathbf{r} - \mathbf{r}_i)$. To distinguish the different substructures, pearls and strings, it is better to use a coarse-grained local monomer concentration, $\rho_m^c(\mathbf{r})$, which is defined as

$$\rho_m^c(\mathbf{r}) = \frac{1}{V_c} \int_{\mathbf{r}' \in V_c} d\mathbf{r}' \rho_m(\mathbf{r}') \quad (7)$$

where V_c is a spherical volume with radius r_c around \mathbf{r} . This observable is larger in a pearl than in a string. One can calculate $\rho_m^c(\mathbf{r})$ along the backbone as a function of the monomer positions \mathbf{r}_j . This is done for a chain with length $N_m = 382$ from series A1, the snapshot of which is shown in Figure 1a. The resulting coarse-grained local monomer concentration with $r_c = 4\sigma$ is shown for comparison directly underneath in Figure 1b.

A second approach uses local distances between the monomers, which could be probed by NMR experiments.³⁰ The local distance between monomer j and the monomer $j + n$, which is n monomers apart on the backbone, is defined as

$$r_n(j) = \sqrt{(\mathbf{r}_j - \mathbf{r}_{j+n})^2} \quad (8)$$

From scaling arguments, one expects that the local distances inside the compact pearls scale with $r_n \approx n^{1/2}$ for small n whereas in the extended strings it scales with $r_n \approx n$. The symbol \approx is used to state a scaling relation that ignores numerical prefactors. For the conformation shown in Figure 1a, the local distances along the backbone are shown for $n = 10$ in Figure 1c.

In both cases, one can see the position of the four pearls and three strings. The problem is that the variation of both $\rho_m^c(\mathbf{r})$ and $r_n(j)$ is of the same order as the difference between the mean values in pearls and strings.

Because the two previous methods have several problems with the structure recognition of pearl-necklace conformations, we have developed a more reliable algorithm based on a simple cluster recognition. The question whether a group of monomers forms a cluster is often connected to a distance criterion, for

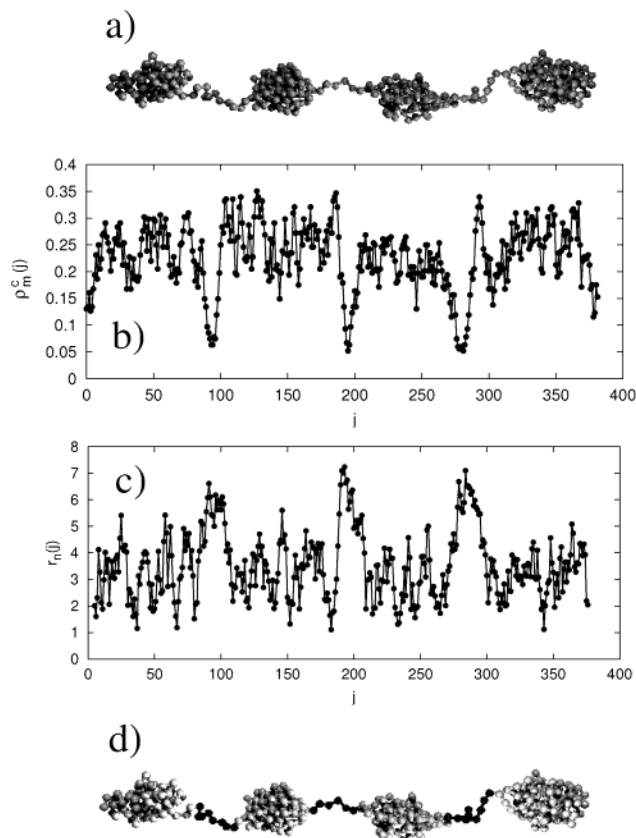


Figure 1. Snapshot (a) of a polyelectrolyte chain with $N_m = 382$ from series A1, (b) coarse-grained local monomer concentration, $\rho_m^c(j)$, with $r_c = 4\sigma$ along the backbone, (c) local distances, $r_n(j)$, for $n = 10$ along the backbone, and (d) analysis with the cluster-recognition algorithm. Monomers in pearls are gray and monomers in strings black.

example, monomers with a distance smaller than a critical value belong to the same cluster. For a polymer, one has also to take into account the chain connectivity. This implies that a pure distance criterion is not sufficient. Therefore, we require in addition that there are a certain number of bonds between a pair of monomers along the chain contour. The resulting algorithm is iterative and contains the following steps: (1) At the beginning, every monomer is a cluster of size 1 (size = number of monomers belonging to a cluster). (2) Two clusters, \mathcal{C}_1 and \mathcal{C}_2 , are merged if they contain a pair of monomers ij with $i \in \mathcal{C}_1, j \in \mathcal{C}_2$ and $r_{ij} < r_c$. In addition, i and j are further apart than n_c bonds along the chain contour, $|i - j| > n_c$. (3) Step 2 is repeated among all clusters as long as one finds clusters that have to be merged. (4) Loops are removed; a cluster \mathcal{C}_1 in which all monomers are inside (along the chain contour) of another cluster \mathcal{C}_2 is merged with \mathcal{C}_2 . Note that this step is only suitable for polyelectrolytes but, for example, is not applicable for polyampholytes. (5) A practical definition of pearls is given as all clusters with a size larger than or equal p_c are pearls. Pearls that are connected directly along the chain contour are merged. (6) A practical definition of strings is given as all clusters with a size smaller than p_c belong to strings. Strings that are connected directly along the chain contour are merged. (7) Dangling ends are removed and merged to the end pearls. We do this because we have so far not seen dangling ends containing more than three monomers, which could be seen as an extra string.

Thus the algorithm has in principle three free parameters: r_c , n_c , and p_c . But looking at the involved structures, one can establish relations between these parameters, which can be used

as a rough guide in choosing them. From scaling arguments, we know that the distance of two monomers i and j with a distance $|i - j|$ along the chain contour scales as $|i - j|^{1/2}$ inside the pearls and as $|i - j|$ inside the strings. Thus, we can choose $bn_c^{1/2} < r_c < bn_c$ to distinguish the two cases. For a weakly charged chain, one can determine a suitable value for p_c with help of the pearl size defined in eq 13. But this is not possible for our strongly charged systems with their subtle dependence on the counterion distribution. The whole data analysis in this paper is done with an empirical parameter set: $r_c = 2.1\sigma$, $n_c = 6$, and $p_c = 9$. Beside extended visual checks, we have tested that small changes of the three parameters do not have a significant effect on the final result. The derived sizes for the substructures contain a systematic error of plus or minus four monomers coming from the two outer monomers on each side of a substructure, for which one cannot decide whether they belong to the next pearl or the next string. A typical result for a structure type with four pearls is shown in Figure 1d. The four pearls and three strings contain the following numbers of monomers: 90–8–94–6–77–9–98. We do not claim that this is the fastest or the best way to identify pearl-necklace structures, but it worked well when compared with visual checks and thus served our purpose. For an average pearl size larger than 30 monomers, it yields a reliability well above 95%.

5. Scaling

One of our goals in this paper is to show to what extent scaling theories that are made for long chains at infinite dilution can be expected to work for dilute PE systems with finite length at finite density. The scaling theory predicts the dependencies of observables such as the chain extension on various parameters, for example N_m , ϵ_B , f , and the reduced temperature τ_r . Here, we give only a short overview of some results of the scaling theory for the pearl-necklace regime of polyelectrolytes. For the pearl-necklace regime, one finds the following relations:^{9,10,17} end-to-end distance R_E ,

$$R_E \simeq N_m b^{1/2} \epsilon_B^{1/2} f \tau_r^{-1/2} \quad (9)$$

number of pearls n_P ,

$$n_P \simeq N_m b^{-1} \epsilon_B^2 f \tau_r^{-1} \quad (10)$$

string length l_S ,

$$l_S \simeq b^{3/2} \epsilon_B^{-1/2} f \tau_r^{1/2} \quad (11)$$

pearl size (radius) r_P ,

$$r_P \simeq b^{4/3} \epsilon_B^{-1/3} f \tau_r^{-2/3} \quad (12)$$

pearl size (number of monomers) g_P ,

$$g_P \simeq b \epsilon_B^{-1} f \tau_r^{-2} \quad (13)$$

density inside the pearls ρ_P ,

$$\rho_P \simeq b^{-3} \tau_r \quad (14)$$

Note that r_P is independent of the solvent quality and that our solvent quality parameter ϵ is proportional to the second virial coefficient of the LJ potential and hence also proportional to the reduced temperature τ_r .

5.1. Scaling Variable Chain Length N_m . The linear scaling of R_E with N_m is caused by the electrostatic repulsion of the

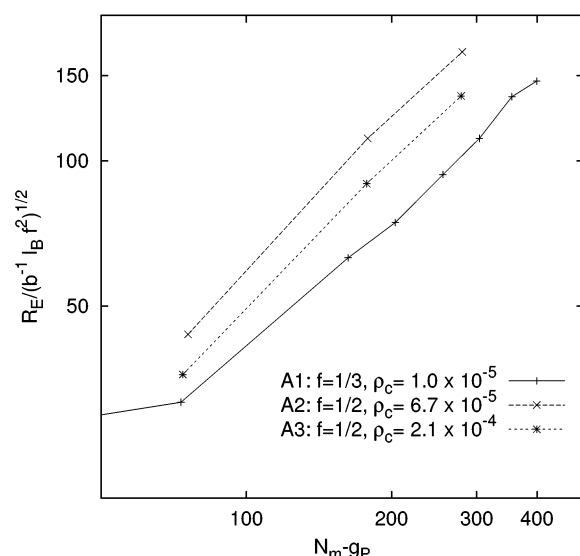


Figure 2. Scaling plot for R_E versus $(N_m - g_P)$ (see eq 9). The series A1, A2, and A3 differ in the charge fraction f and the density ρ_c . One can see that R_E scales linearly with $(N_m - g_P)$, but the prefactor is not constant.

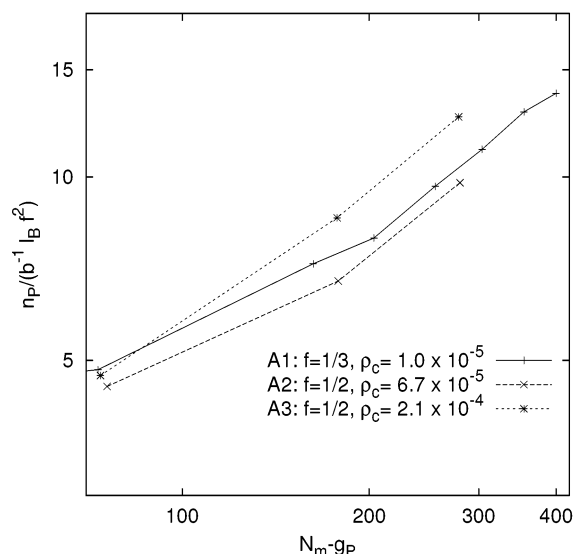


Figure 3. Scaling plot for n_P versus $(N_m - g_P)$ (see eq 10) for series A1, A2, and A3.

chain charge and is dominated by the string length l_S . Because of the finite length of our systems, we have to correct the scaling relation given in eq 9. For small chain length, $N_m \leq g_P$, the chain conformation consists of one pearl. The size of this pearl scales as $N_m^{1/3}$. Thus, we have to replace N_m by $(N_m - g_P)$ in eq 9. In Figure 2, a linear relation between R_E and $(N_m - g_P)$ can be observed. But the full scaling relation from eq 9 including the parameters specifying the Coulomb interaction, namely, f , is not valid. Series A1 is performed at $f = 1/3$, and its density is between that of series A2 and A3, which have both $f = 1/2$.

We find a similar result for the number of pearls n_P in the pearl-necklace regime. The scaling relation for n_P versus $(N_m - g_P)$ (see eq 10) is shown for the data from series A1, A2, and A3 in Figure 3. Again there is a linear relation between n_P and N_m but different prefactors for different values of f and ρ_c .

To get some visual impression, we show in Figure 4 some snapshots from simulations with different chain length N_m from series A1. The discreteness of the pearl number n_P does not play a significant role for sufficiently long chains, which give

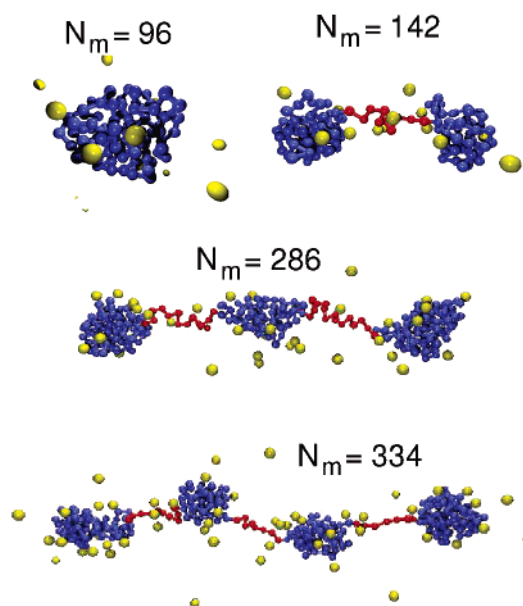


Figure 4. Snapshots from series A1 with different chain length N_m and different number of pearls n_P .

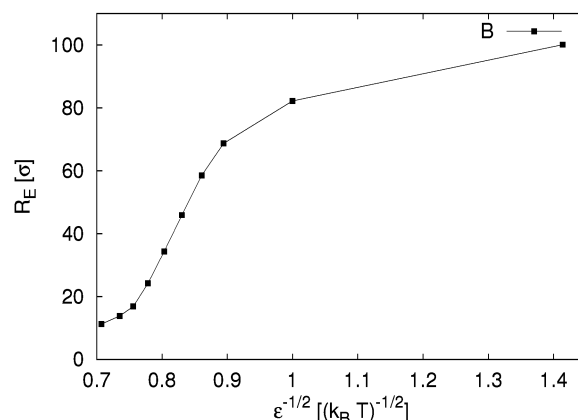


Figure 5. Dependence of R_E on the solvent quality parameter ϵ (simulation series B).

rise at least to a dumbbell. Then our data is in accord with the scaling relations for the quantities pearl size, string length, and pearl density; namely, they are constant within the statistical error. We find the following for the systems of series A1 with $N_m > 200$: $g_P = 78 \pm 4$, $\rho_P = (0.67 \pm 0.04)\sigma^{-3}$, and $l_S = (7.3 \pm 2)\sigma$. As we will show later, the discreteness of the number of pearls is smeared out because of fluctuations between different structure types in a way that the average quantities can maintain their optimal values; compare also section 6.

5.2. Solvent Quality ϵ . In the simulation series B, we have tested the behavior of polyelectrolyte chains upon changing the solvent quality via the Lennard-Jones parameter ϵ . Because the practically usable range for this parameter is small, ranging from $\epsilon = 0k_B T$ to $2.0k_B T$, it is not possible to test the scaling predictions over a large parameter range. In addition, the range of ϵ values for which we observed pearl-necklace structures is even smaller, namely, from $\epsilon = 1.0k_B T$ to $2.0k_B T$. For values of $\epsilon < 1.0k_B T$, one leaves the poor-solvent regime, and for values $\epsilon > 2k_B T$, we encounter simulation problems, for example, kinetically frozen states.

The dependence of R_E and n_P on ϵ is shown in Figures 5 and 6. For both observables, the scaling predictions seem to hold for a small ϵ region. R_E scales linearly with $\epsilon^{-1/2}$ in the range from $\epsilon = 1.25k_B T$ to $\epsilon = 1.75k_B T$ (see eq 9). The regime in

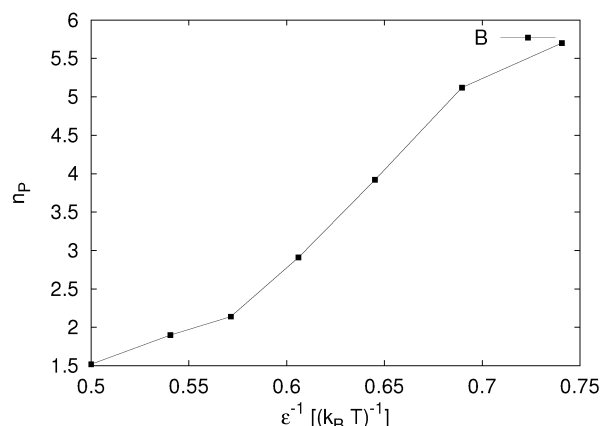


Figure 6. Dependence of n_p on the solvent quality parameter ϵ (simulation series B).

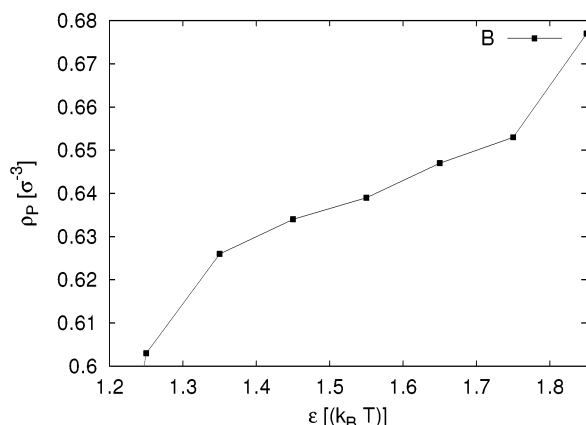


Figure 7. Dependence of ρ_p on the solvent quality parameter ϵ (simulation series B).

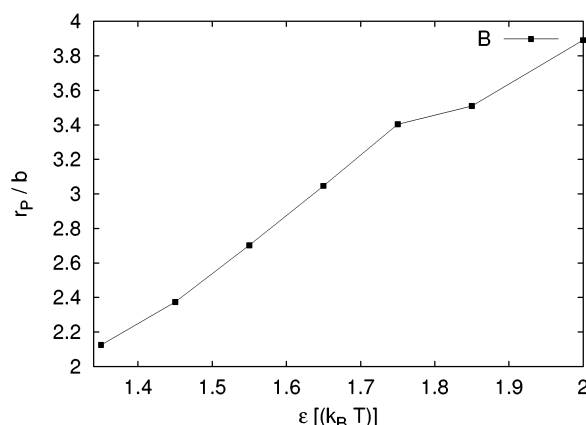


Figure 8. Dependence of r_p on the solvent quality parameter ϵ (simulation series B).

which n_p scales as ϵ^{-1} is even smaller and extends from $\epsilon = 1.45k_B T$ to $\epsilon = 1.75k_B T$ (see eq 10). In the same regime, also the density inside the pearls ρ_p , which is plotted against ϵ in Figure 7, shows a linear dependence on ϵ as predicted by eq 14. However, a more reliable conclusion may be drawn from the scaling relation for the pearl size r_p , because r_p should be independent of the solvent quality (see eq 12). We therefore have calculated the pearl size as $r_p = \sqrt[3]{\frac{3}{4}\pi g_p \rho_p^{-1/3}}$ from our simulation data and plotted it versus ϵ . As can be seen in Figure 8, r_p increases monotonically with ϵ and hence shows an unexpected dependency on ϵ . We are lead therefore to conclude that the scaling predictions for the dependency on the solvent quality do not work here. They fail for the most definite test

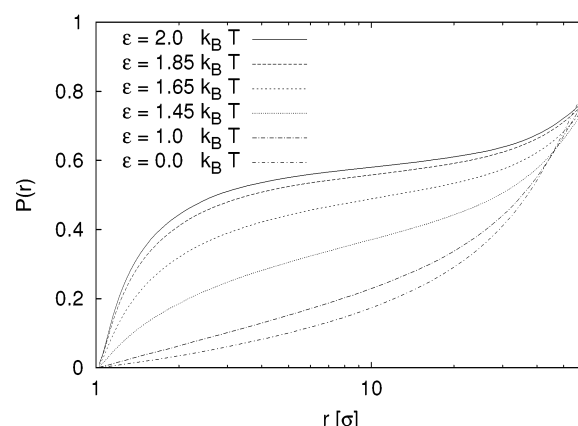


Figure 9. Integrated counterion distribution, $P(r)$, around polyelectrolyte chains subject to different solvent qualities.

case, the independence of the pearl radius r_p of the solvent quality. Nevertheless, in a small regime for $\epsilon/(k_B T) = 1.45 - 1.75$, they seem to work approximately for some observables due to a fortuitous error cancellation.

To elucidate the role of the finite counterion density around the chains, we calculated the integrated ion distribution $P(r)$ (see eq 6). In Figure 9, $P(r)$ is shown for different solvent qualities. The counterion distribution changes greatly close to the chain with ϵ . In the pearl-necklace regime between $\epsilon/(k_B T) = 1.0$ and $\epsilon/(k_B T) = 1.85$, which is the same regime in which we find also the strongest change in the chain extension, we observe that the counterion distribution is changing the most. The fraction of counterions being very close to the chain, which hence can be called condensed, is also varying strongly. Only the top four curves show an inflection point, which is a sign of counterion condensation^{42,43} (see also section 6.1). Scaling theory assumes usually that the counterion condensation depends only on the Manning parameter, $\xi = \ell_B^{-1} f$, and is hence supposed to be independent of the actual conformation of the chain. Note that the total series B is performed at $\xi = 0.5$ and is thus expected to show no counterion condensation at all according to the standard Manning–Oosawa^{44,45} concept, which requires $\xi \geq 1$.

5.3. The Coulomb Parameters: ℓ_B and f . As we demonstrated in the previous subsection 5.2, the interplay between counterions and chain conformation influences greatly the behavior of PEs in poor solvent. Therefore also a thorough investigation of the parameters determining the Coulomb interactions is necessary. This section treats the simulation series C1, C2, and C3 in which we have investigated the ℓ_B dependence but using different charge fractions, $f = 1$ (C1), $f = 1/2$ (C2), and $f = 1/3$ (C3). All simulations are performed at the same charge density, ρ_c . We remark that the valences of the charged particles is yet another important independent parameter. But because this is also not included in the scaling picture and would even further complicate the picture, we will leave this for another study. We will also look at the behavior of these systems with regard to parameters combined of ℓ_B and f , namely, the Manning parameter ξ and the scaling variable, $\ell_B b^{-1} f^2$. The Manning parameter is important for the electrostatic field that counterions would experience around a long stretched chain, and its value determines in a first approximation the onset of counterion condensation. In the framework of scaling theory, simulations performed at the same value of $\ell_B b^{-1} f^2$ should be identical. Nevertheless, our simulations show a big difference between the three series. The dependence of R_E on ℓ_B is shown in Figure 10 and that on n_p in Figure 11. Only for very small values of

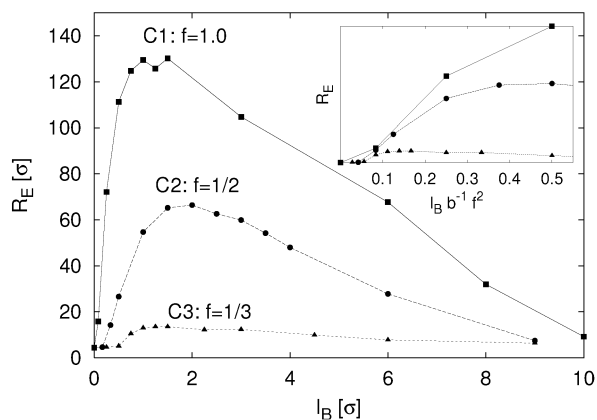


Figure 10. Dependence of R_E on the Bjerrum length, l_B , for the series C1, C2, and C3. The inset shows the dependence of R_E on the scaling variable, $l_B b^{-1} f^2$.

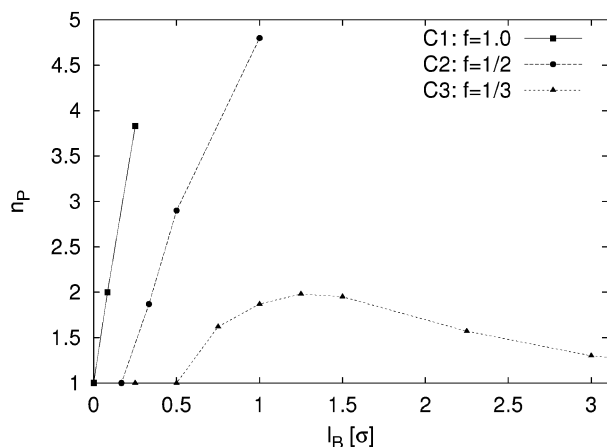


Figure 11. Dependence of n_P on the Bjerrum length, l_B , for the series C1, C2, and C3.

l_B , the counterions and their interaction with the chain conformation do not play a significant role. The prediction from scaling theory (see eq 9) is that our data should collapse on a single master curve. However, our data show that this is only true if the scaling variable $l_B b^{-1} f^2$ is smaller than 0.1. This can be seen in the inset in the upper right corner of Figure 10, where we plotted the same data versus $l_B b^{-1} f^2$. Upon a further increase of $l_B b^{-1} f^2$, the values of the end-to-end distances diverge rapidly. Whereas the chains of series C3 ($f = 1/3$) already start to shrink at $l_B b^{-1} f^2 = 0.15$, the chains of the other series still expand.

The different values of f can be seen as different schemes for the discretization of the backbone charge. This has an effect on the correlations between the charges, which influences the chain conformation and thus also the counterion distribution. In Figure 12, we have therefore plotted the integrated counterion distribution $P(r)$ for several values of the Manning parameter ξ for series C2 and C3. Already the curves for $\xi = 0.5$, which correspond to $l_B = 1\sigma$ for series C2 and $l_B = 1.5\sigma$ for series C3, show a pronounced difference in $P(r)$. Even though the effect of f on the charge–charge correlations may be small, it is enhanced strongly by the interplay between the chain conformation and the counterion distribution. When the counterions only slightly move toward the chain because of correlation effects, the effective charge of the chain will shrink and so does the end-to-end distance. A higher effective Manning parameter, $\xi_{RE} = Q_P b / R_E$, follows, which again attracts more counterions toward the chain. The same holds for the opposite way. This is the same mechanism that we have already seen for the dependence on ϵ in the previous section. The difference

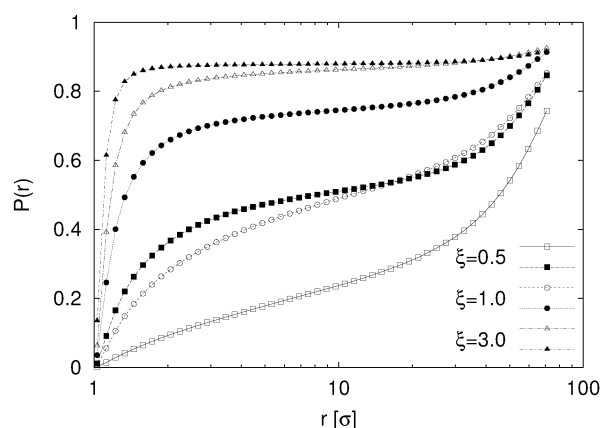


Figure 12. Integrated counterion distribution, $P(r)$, around polyelectrolyte chains for different ξ -values. Open symbols show data from series C2 with $f = 1/2$ and filled symbols from C3 with $f = 1/3$.

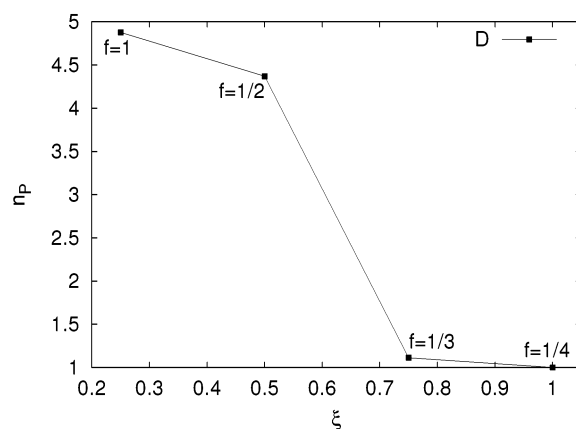


Figure 13. Dependence of n_P on the Manning parameter ξ for the simulation series D with constant scaling parameter $l_B b^{-1} f^2 = 0.25$.

in $P(r)$ becomes smaller with increasing ξ , which is due to the gradual collapse of the polyelectrolyte chain, because then in all cases most of the counterions are close to or even inside the chains.

In series D, we have performed four simulations with $l_B b^{-1} f^2 = 0.25$ but different values for l_B and f . In Figure 13, we show the behavior of n_P as a function of ξ . Decreasing f and thus increasing l_B has again a drastic effect on the chain conformation leading to collapse of the chains for large l_B and small f . Even though the number of pearls for the two first points with $f = 1$ and $f = 1/2$ do not differ much, the chain extension shows a large difference, namely, $R_E = 59\sigma$ for $f = 1$ and $R_E = 32\sigma$ for $f = 1/2$. This is also reflected in a large difference of the pearl sizes and the string lengths. The difference between the systems can again be traced to a quite different distribution of the counterions, as can be inspected in Figure 14 in which we show $P(r)$ for three of the simulations of series D. It is really surprising that such a small change, basically in the discretization of the charges, has such a big impact on the chain conformations. This again shows that the delicate balance between repulsive and attractive forces is very sensitive to subtle changes. These effects are definitely not captured by the parameter $l_B b^{-1} f^2$, which is used in scaling theories. We will come back to the collapse discussion in section 7 in which we will also give an overview of the occurring conformations.

6. Fluctuations

The data analysis shows that pearl-necklace conformations are very soft objects that display large fluctuations on all length

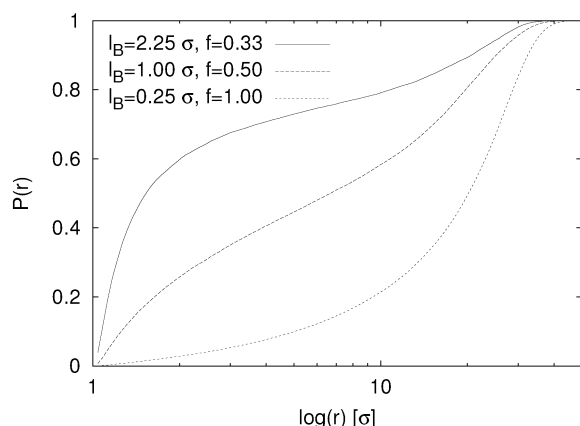


Figure 14. Integrated counterion distributions, $P(r)$, for different charge fractions f with constant $l_B b^{-1} f^2 = 0.25$ (series D).

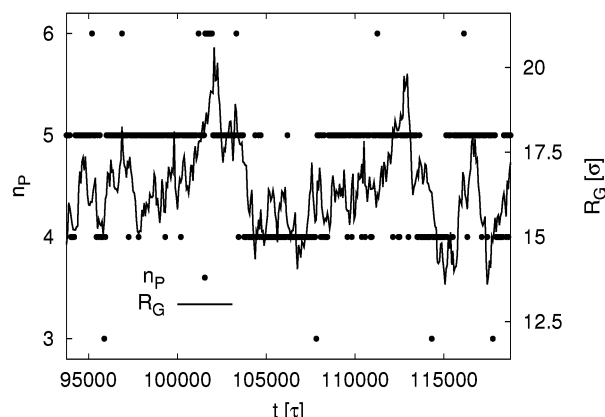


Figure 15. Time evolution of the structure type (number of pearls) and the radius of gyration R_G of a single chain ($N_m = 382$, series A1).

scales. We will measure in detail the extent of the various fluctuations because this is important for the interpretation of experimental measurements on polyelectrolyte solutions (see section 8).

6.1. Fluctuations of the Structure Type—Coexistence. In most of our simulated systems, we find coexistence of pearl necklaces with different number of pearls, which we call structure types. It is important to note that the observed coexistence is not caused by frozen metastable states. We have excluded this possibility by observing individual chains over a larger period of time each showing a large number of transitions between different structure types during the simulation time. The typical time evolution of the structure type n_P and the radius of gyration R_G for an individual chain is exemplarily shown in Figure 15. In this case, the chain mainly fluctuates between structures with four and five pearls, but we also see a significant fraction of structures with three and six pearls. Looking at R_G , one can see a certain correlation with the structure type, which is reflected also in the mean value for different structure types: $R_G^{(3)} = (14.7 \pm 1.3)\sigma$; $R_G^{(4)} = (16.1 \pm 1.5)\sigma$; $R_G^{(5)} = (17.5 \pm 1.6)\sigma$; $R_G^{(6)} = (19.5 \pm 1.7)\sigma$. Here and in the following, the superscript denotes that an observable is measured only for conformations with a certain number of pearls, n_P . But nevertheless such a simple chain observable is not suited for structural discrimination, as one can see from the given mean deviations. The same holds for other chain observables such as R_H and the characteristic ratios r and α .

One could be tempted to explain the coexistence of two structure types by a simple finite size argument, namely, that the ratio of N_m and the optimal pearl size g_P is not always an

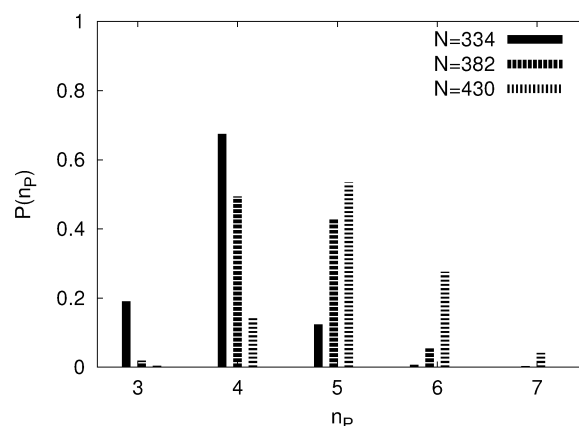


Figure 16. Probability distribution for the structure types found in systems with different chain length from series A1.

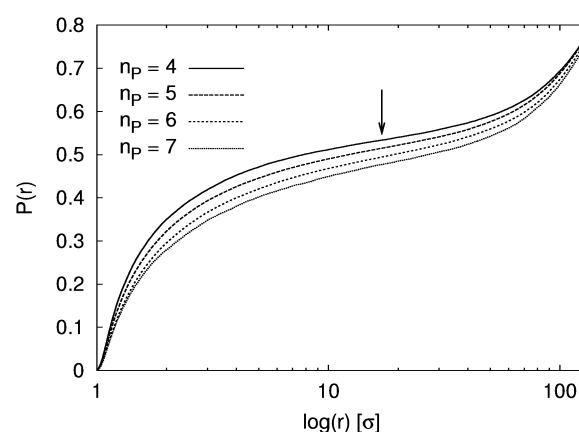


Figure 17. Integrated counterion distributions, $P(r)$, for different structure types for the system with $N_m = 430$ from series A1. The arrow pointing to $(17\sigma, 0.53)$ shows the position of the inflection point for the structure type with $n_P = 4$.

integer. In Figure 16, we plot the probability distributions $P(n_P)$ of the structure types for three different chain lengths. We clearly observe a coexistence range containing up to four different structure types. This means that the different observed structure types can only have small differences in the free energy of the order of the thermal fluctuation spectrum. To confirm this, we calculate from the shown probability distribution the free energy differences between structure types with n and m pearls according to the Boltzmann factor:

$$\frac{\Delta \mathcal{F}^{(nm)}}{k_B T} = \frac{\mathcal{F}^{(n)} - \mathcal{F}^{(m)}}{k_B T} = \ln \frac{p^{(n)}}{p^{(m)}} \quad (15)$$

For the case with $N_m = 430$, we find $\Delta \mathcal{F}^{(45)} = -1.32 k_B T$, $\Delta \mathcal{F}^{(56)} = 0.66 k_B T$, and $\Delta \mathcal{F}^{(67)} = 1.9 k_B T$. All values are on the order of $k_B T$, which is consistent with our observed large coexistence regime.

As we will argue, these small differences in the free energy between different structure types are mainly due to the interplay of the counterion distribution and the chain conformation. To elucidate the role of the counterions, we look at the counterion distribution around the PEs analyzed for each structure type separately. In Figure 17, we have plotted the integrated counterion distributions $P(r)$ for different structure types for the system with $N_m = 430$ from series A1. One observes more counterions to be close to the chains with a smaller pearl number. This can be easily understood if one looks at the far electrostatic field of the chain. For distances larger than the

pearl–pearl separation, r_{pp} , the chain can be seen as a charged cylinder with an effective Manning charge parameter, $\xi_{RE} = Q_{pb}/R_E$. The end-to-end distance increases with increasing pearl number: $R_E^{(4)} = 48.8\sigma$, $R_E^{(5)} = 54.1\sigma$, $R_E^{(6)} = 60.1\sigma$, and $R_E^{(7)} = 64.0\sigma$; hence, the shorter chains have a larger effective Manning charge parameter, namely, $\xi_{RE}^{(4)} = 2.95$, $\xi_{RE}^{(5)} = 2.67$, $\xi_{RE}^{(6)} = 2.40$, and $\xi_{RE}^{(7)} = 2.25$.

Because the PEs in this regime are elongated structures and they carry a large effective line charge, it might be worthwhile to compare the ion distribution with predictions from Poisson–Boltzmann (PB) theory. This is also supported by the functional form of the integrated counterion distributions in Figure 17, which looks very similar to that of an infinitely charged rod within the cell model.⁴⁶ In the framework of the PB theory applied to the cell model for an infinitely long charged cylinder,⁴⁷ one can calculate the fraction f_c of Manning–Oosawa condensed counterions^{44–46} as $f_c = 1 - (1/\xi)$. In the simulation, the fraction of condensed counterions can be read off as the value of $P(r)$ at which the $P(r)$ curve, plotted as a function of $\log(r)$, has an inflection point. Using $\xi = \xi_{RE}$, we find for the $n_p = 4$ structure that the cell model prediction for $f_c = 0.66$ is higher than the value that can be read off the inflection point criterion, that is, $f_c = 0.53$. A perfect quantitative agreement can however not be expected because our system is finite and has as such a smaller electric field and second the pearl-necklace structures do alter the near electrostatic field of the chain and lead to an inhomogeneous counterion distribution. As a word of caution, we remark that the bare value for the Manning parameter of the chain in Figure 17 is 0.5, which would not lead to any counterion condensation at all in the simple Manning picture, and the functional form of an infinite rod with that charge value would simply not show any inflection point. This again demonstrates that poor-solvent chains, because of the short-range attraction between monomers, feature a higher effective charge density. Because the Poisson–Boltzmann cell model can at least qualitatively explain the change in the counterion distributions a more refined version of this model seems to be necessary. A possible starting point could be to combine the PB rod and sphere geometry as has been suggested in ref 48.

When more counterions are near the chain, we find, in terms of a charge renormalization, that the effective line charge density of the chain decreases. This allows the chain to contract further, which itself induces a stronger counterion attraction. Again a lower effective line charge density also increases the optimal pearl size. This results in shorter chains with fewer pearls. The opposite, longer chains with more pearls, holds when the counterions move away from the chain. This lowers the difference in the free energy between the different structure types, as was suggested above.

Scaling theories have predicted a collapse of the pearl-necklace structure into a globule as soon as counterion condensation starts^{9,10,49,50} due to an avalanche behavior of condensing counterions that contracts the chain. In the investigated parameter range where we observe stable pearl-necklace conformations in our simulation data, we did not see such a collapse transition. In light of a recent study,⁵¹ this is not surprising because it can be shown that this collapse depends on how easily the counterions can enter the globule, the ion concentration, and the strength of the electrostatic interaction. Also the necessary amount of condensed counterions to induce the collapse can be quite high.

We also suggest that the fluctuations due to the presence of the counterions lower the energy barrier between the different

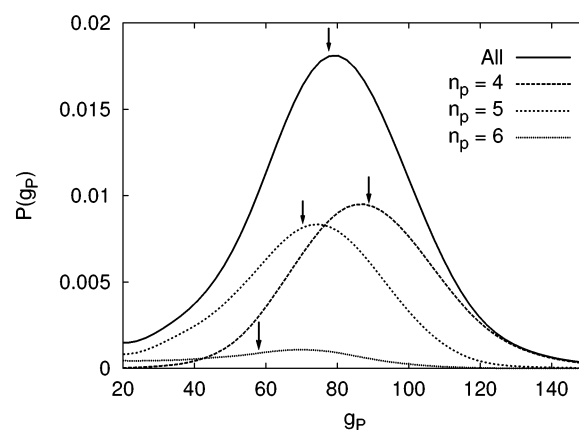


Figure 18. Probability distributions P for the pearl size g_p for the system with chain length $N_m = 382$ from series A1. Shown is the distribution for all chains, as well as the distributions for the different structure types. The arrows mark the mean value of the corresponding probability distribution.

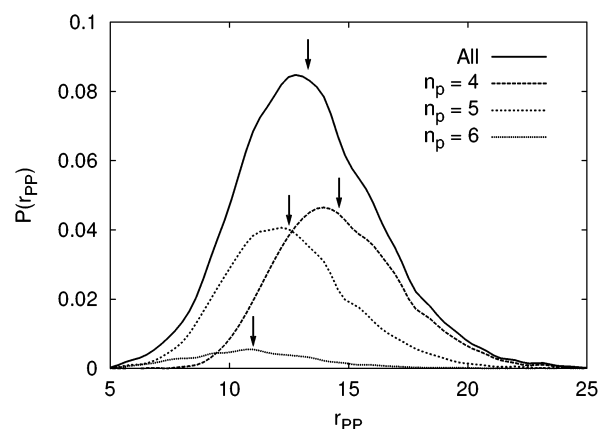


Figure 19. Probability distributions P for the pearl–pearl distance r_{pp} for the system with chain length $N_m = 382$ from series A1. Shown is the distribution for all chains, as well as the distributions for the different structure types. The arrows mark the mean value of the corresponding probability distribution.

structure types. To confirm this suggestion, one would need to analyze the transition frequency between the different structure types for chains with explicit counterions and a corresponding Debye–Hückel chain with the same n_p . This is however outside the scope of the present investigations.

6.2. Fluctuations of the Substructures. In this section, we discuss fluctuations of the chain conformation on a smaller length scale, namely, the radius of the pearls, r_p , and the pearl–pearl distance, r_{pp} . The probability distributions for the pearl size, g_p , are shown in Figure 18 and for the pearl–pearl distance, r_{pp} , in Figure 19. Both distributions are quite broad. The relative standard deviations for the distributions of all chains are $\delta g_p = 0.32$ and $\delta r_{pp} = 0.22$.

As we have already seen for the overall chain extension, also the size of the substructures are influenced by the counterion distribution. The pearl size is decreasing with increasing number of pearls and increasing chain extension, as one can see from the arrows in Figure 18. Still an explanation in terms of a charge renormalization is not sufficient for an understanding. This becomes more clear when we look at the number of counterions inside a shell around the chains. When these numbers are rounded to integers, we find for a shell radius of 3σ on average 56 counterions. When these numbers are averaged separately for the different structure types, we find 60, 57, 53, and 50

counterions for structures with four, five, six, and seven pearls. It is interesting to note that the difference in this number of counterions is roughly constant for shells with radii ranging from 2σ up to 30σ and is thus independent of the exact definition of counterions called “condensed” to the chains. Thus we now use a practical definition of an effective charge using the counterions that are closer than 3σ to the next monomer. For the example, this yields an effective pearl charge of 18, 15, 13, and 11 charges for structures with four, five, six, and seven pearls, respectively. Because the pearl size is only slowly varying one gets large differences in the electrostatic self-energy of the pearls of different structure types.

In the scaling Ansatz, the distance between neighboring pearls, r_{pp} , is determined by the balance between the electrostatic repulsion between the chains and the energy one needs to pull monomers out of the pearls. The second term is related to the surface tension and is roughly constant. The term connected to electrostatics is more complex. We approximate it by the electrostatic energy of two point charges carrying the average pearl charge, separated by the average pearl–pearl distance. The value of r_{pp} ranges from 15.4σ for four-pearl structures to 11.1σ for seven-pearl structures. Together with the above calculated effective pearl charges, we can estimate the electrostatic repulsion between neighboring pearls to be $31.9k_B T$ for four-pearl structures and $16.7k_B T$ for seven-pearl structures. Note that we neglect the energetic contribution of the other pearls. This difference can also not be explained by a standard Debye–Hückel potential because the Debye screening length, calculated from the bulk charge density $\rho_c = (1 \times 10^{-5})\sigma^{-3}$ in the system, is $\lambda_D = 72.8\sigma$ and is thus much larger than the values for r_{pp} . Of course, closer to the chain, the counterion density is much larger than that in the bulk, which could be a hint to explain the observed differences. The counterion density is rapidly varying with the distance from the chain starting with $\sim 10^{-1}\sigma^{-3}$ at a distance of 1.5σ and dropping below the bulk density at a distance of 50σ .

The electrostatic self-energy of the pearls and the electrostatic pearl–pearl repulsion show explicitly the discrepancies between a mean-field approach and our simulation results. It also clearly demonstrates that it is necessary to include the counterion distribution into the model. Moreover correlations between the counterions and the chain charges seem to play an important role. For instance, it can be shown that the counterions preferentially accumulate between the pearls. Because the structure of polyelectrolytes in poor solvent turns out to be extremely sensitive to the inhomogeneities of the counterion distribution, it should be used as a test case for the development of theoretical approaches beyond the mean-field level. A more detailed discussion of these inhomogeneities can be found in refs 21 and 52.

7. The Sausage Regime and Phase Space

To get an overview of the parameter regimes through which our different simulation series are scanning, we have depicted them in a phase plot for polyelectrolytes using the parameters ϵ and ℓ_B^{-1} , as it was done, for example, in ref 10. Some of the simulation series are marked with dashed lines in Figure 20a. Close to the lines, we have put some snapshots of the configurations to get a visual impression.

Looking at series C3 crossing the entire ℓ_B range, we find, starting on the right side at the neutral case with $\ell_B = 0.0\sigma$, a neutral globule. The chain is collapsed due to the poor solvent. With increasing ℓ_B , the chain is getting charged, the self-energy grows, and we can observe the Rayleigh instability at $\ell_B = 0.75\sigma$

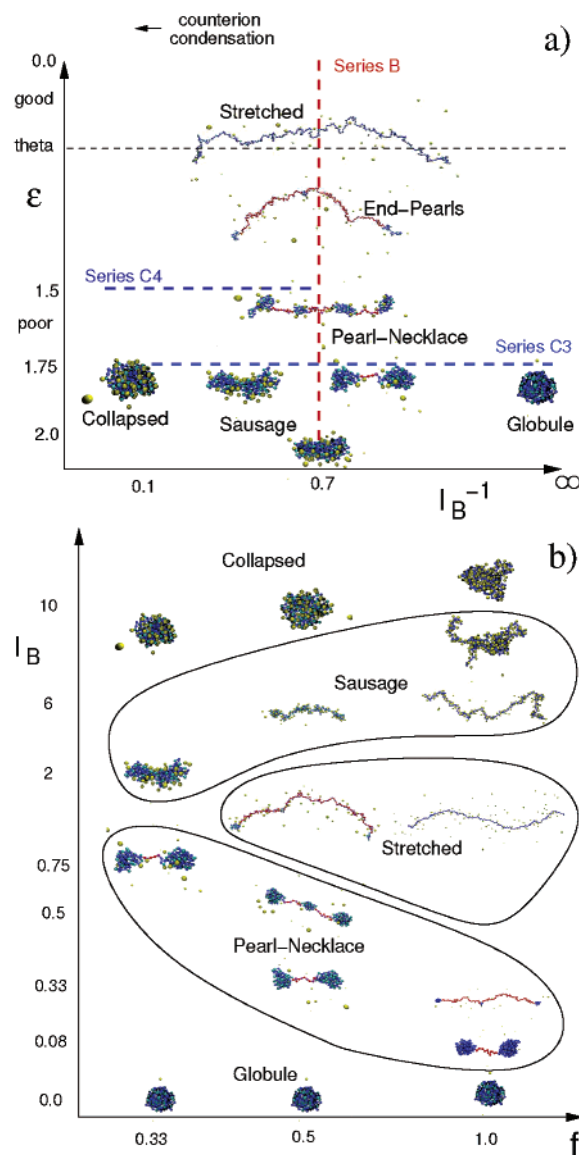


Figure 20. Schematic views of the location of the different PE configuration types: (a) In the ϵ/ℓ_B^{-1} phase diagram, all simulations are performed at $f = 1/3$, and the dashed lines indicate the location of the simulation series B, C3, and C4; (b) in the ℓ_B/f phase diagram, the simulations are from series C1 at $f = 1$, C2 at $f = 1/2$, and C3 at $f = 1/3$ performed at $\epsilon = 1.75k_B T$.

where the globule splits into a dumbbell. At this point, we find already some counterions close to the chain; hence, there are condensed counterions present. Further increase of ℓ_B can lead to further Rayleigh instabilities, depending on the parameters. Then, after reaching its maximum extension at $\ell_B = 1.25\sigma$, the chain slowly shrinks because the enlarged Coulomb repulsion gets overcompensated by condensing counterions. Finally, we reach a collapsed conformation at $\ell_B = 9.0\sigma$. The nonmonotonic behavior of the chain extension is qualitatively the same as that in the good-solvent case and qualitatively well understood,^{10,53,54} however, the decrease is faster and more pronounced in the poor-solvent case.^{19,55}

Scaling theories have predicted that with the onset of condensation the pearl necklace should collapse in a first-order transition.^{9,10,49,50} However, we find always a smooth distribution of counterions that looks like a distribution that can be calculated within PB theory.⁴³ The counterions get pulled closer to the macroion as the Coulomb coupling is increased, and a rather high Bjerrum length, or similarly, a large number of condensed

counterions are needed to collapse the PE to a globule. Also the osmotic pressure does not show any dramatic decrease with ℓ_B , so we believe that for an adequate description of the collapse we need a refined theory.

A very interesting, and as we believe, new conformational regime opens up basically for those ℓ_B values between the maximal chain extension up to the collapsed state. Here, we find conformations that are reminiscent of a cigar-like shape⁴⁹ but turn out to look more like a sausage for longer chains. Because with increasing ℓ_B more counterions are attracted toward the chain, the pearl–pearl repulsion is getting screened such that the pearls slowly coalesce and the conformation is not stretched on longer length scales anymore. Because of its shape, we have termed it the sausage regime. Note that the actual conformation depends also on f where smaller values of f lead to thicker sausages. Conformational snapshots are shown in Figure 20b.

At the crossing point of series B and C3 at $f = 1/3$, $\ell_B = 1.5\sigma$, and $\epsilon = 1.75k_B T$ being in the pearl-necklace regime, we have studied the N_m dependence of the chain conformation. Starting from short chains, which form a globule, for example, one pearl, we enter a number of Rayleigh instabilities upon elongation. A few exemplary snapshots of series A1 have already been shown in Figure 4.

As a next step, we have studied the dependence of the conformations upon the charge fraction f . As one can see in Figure 20b, this opens up a completely new plane in the phase diagram of polyelectrolytes. The three simulation series C1, C2, and C3 all scan the entire ℓ_B range and differ only in the charge fraction f .

In mean-field theories for polyelectrolytes, we find two important parameters. The first one is the Manning parameter, $\xi = \ell_B b^{-1} f$, which plays a role in all attempts to renormalize the charge of highly charged polyelectrolytes.⁴⁴ The second one is a measure for the overall Coulombic repulsion on a charged chain, $\ell_B b^{-1} f^2$. As a first Ansatz for a scaling theory for highly charged polyelectrolytes at finite density, an effective charge fraction, $f_{\text{eff}} = (f/\xi)$, is often used, trying to combine both parameters. In this framework, the three simulation series should behave identically. In contrast to this we find, for example, that the maximal extension $R_E(\text{max})$ for the three series differs strongly. Namely, we find for C1 $R_E(\text{max}) = 130\sigma$, for C2 $R_E(\text{max}) = 66.4\sigma$, and for C3 $R_E(\text{max}) = 13.5\sigma$. It is also striking that only the series with larger f has a regime in which the chains are stretched and they behave as if they were in a good solvent.

The Rayleigh instability occurs at the same value, $\ell_B b^{-1} f^2 \approx 1/12$, for all three series, as expected because the counterions do not play a dominant role here. When ℓ_B is increased from this point on, the three series behave very differently. Whereas the series with $f = 1/2$ and $f = 1$ show a cascade of Rayleigh instabilities budding more pearls until they reach stretched conformations, the series with $f = 1/3$ has a dumbbell conformation at the maximum extension. The maximum extension itself is reached at different values for ℓ_B (see Figure 10). For series C1, the maximum extension is probably more restricted by the chain entropy than that is determined by the interplay between repulsive and attractive interactions. The chains then slowly shrink and enter the sausage regime. Still at the same value of ℓ_B , the chains with $f = 1$ are much longer than the chains with $f = 1/2$ or $f = 1/3$. Finally the collapsed conformation is reached roughly at the same value of $\ell_B \approx 8\sigma$. In this regime, we have almost a dense electrolyte solution with mobile ions inside the chains, so we should be close to the critical behavior of a

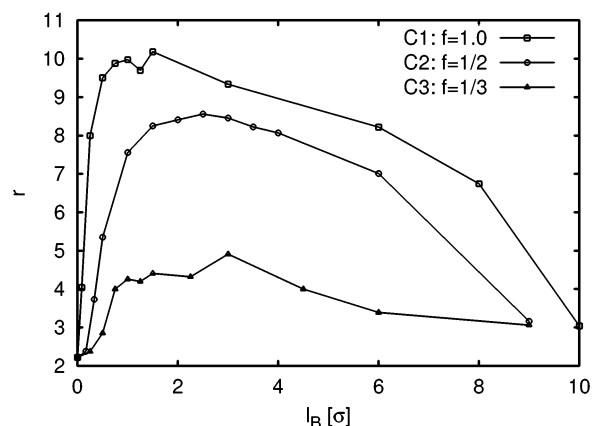


Figure 21. Change of the characteristic ratio r with ℓ_B for different f (series C1, C2, and C3).

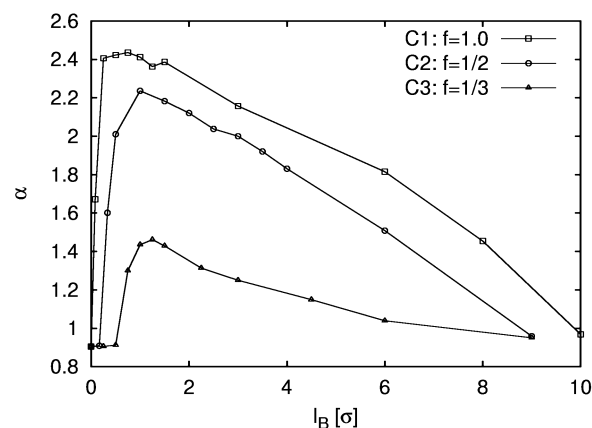


Figure 22. Change of the characteristic ratio α with ℓ_B for different f (series C1, C2, and C3).

Coulomb fluid. This suggests that the collapse should occur at roughly the same value of the coupling parameter, $v_m v_c \ell_B / \sigma$, which is the interaction energy of two oppositely charged ions at contact in units of $k_B T$.

In principle, the phase space for polyelectrolytes has far more than the shown three dimensions. As we know from previous studies,^{19,22–24,36} also the density is a very relevant parameter and would have to be included into the phase diagram. Further important parameters are the valency of the counterions and added salt concentrations, which we did not investigate at all here. This all reflects the fact that there is presumably no general parameter for the Coulomb interaction.

8. Chain Conformation and Experiments

The last section focuses on the connection between the chain conformation and experimentally accessible observables such as the characteristic ratios r and α and the form factor S_1 .

8.1. Characteristic Ratios. The characteristic ratios $r = (R_E/R_G)^2$ and $\alpha = R_G/R_H$ are often used as a first step to characterize conformations that are extended in one dimension. Because both R_G and R_H are accessible with experimental methods, it is interesting to know how α can be used to distinguish different conformation types.

In Figures 21 and 22, we show the change of the characteristic ratios r and α with ℓ_B for the series C1, C2, and C3, for example, for different f . For the globular conformation at $\ell_B = 0\sigma$, we find $r \approx 2.2$ and $\alpha \approx 0.9$. For dumbbells, we find values for r between 4 and 4.5 and $\alpha \approx 1.6$. With further increase of ℓ_B , both observables reach a maximum roughly at the maximal

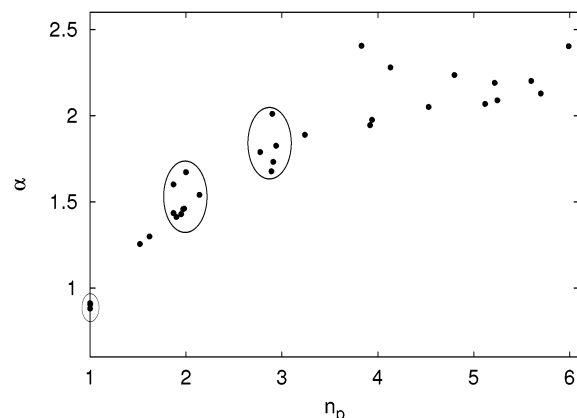


Figure 23. Characteristic ratio α for pearl-necklace structures as function of n_p . The ellipses combine points close to $n_p = 1, 2$, and 3 .

chain extension (compare to Figure 10). Then r and α decrease monotonically until the collapsed conformation is reached at high values of l_B where we find $r \approx 3$ and $\alpha \approx 1$. For a globular object, one can calculate r to be between 2 and $10/3$ which is consistent with our findings. For a completely stretched object one would have $r = 12$, which is of course not reached with the simulations. The form of the shown curves for r and α clearly indicates that it is not possible to deduce the conformation type because at each value the chain could either be in a pearl-necklace conformation or, at higher l_B , in a sausage-like conformation.

Because for the pearl-necklace regime itself α is a monotonic function of n_p , we have plotted the values of α for all simulations in this paper that we assign to this regime in Figure 23. One can see a clear jump of α between $n_p = 1$ and $n_p = 2$. But the range of α between conformations with two and three pearls are already overlapping. With increasing n_p , the slope of $\alpha(n_p)$ is decreasing and a further structure discrimination is not possible. So even in the pearl-necklace regime, it is problematic to use α to discriminate pearl-necklace conformations with different numbers of pearls.

8.2. Form Factor. More information about the chain conformation is contained in the form factor S_1 (see eq 5). In Figure 24, we show $S_1(q)$ for different simulations from series C2. The figure shows the form factors for the different conformation types that we have found in our simulations, namely, the neutral globule, the dumbbell, the three-pearl conformation, stretched chains, sausage-like conformations, and a collapsed chain with most of the counterions being inside.

The neutral globule shows Porod scattering. The strong oscillations show that the globule has sharp boundaries and does not fluctuate strongly. $S_1(q)$ for the dumbbell exhibits a shoulder at $q \approx 0.5\sigma^{-1}$ corresponding to a length of $\sim 12.5\sigma$ that can be identified as the distance between the two pearls. The strong decrease at higher q -values indicates again a Porod scattering in this case coming from the surface of the pearls. The minima of the Porod scattering are smeared out by fluctuations of the shape and size of the pearls. For the three-pearl conformations, we find two shoulders, one at $q \approx 0.2\sigma^{-1}$ and one at $q \approx 0.4\sigma^{-1}$. They are also indications of the pearl–pearl distances. But the shoulders here are already less pronounced than those in the case of the dumbbell. The stretched conformation has a qualitatively different $S_1(q)$ showing a scaling with q^{-1} over a large q -range. It follows that the chain is stretched on length scales larger than 10σ up to its full length of 66σ . For the sausage-like conformation, we cannot identify any scaling regime or other signatures. Thus we cannot obtain another length

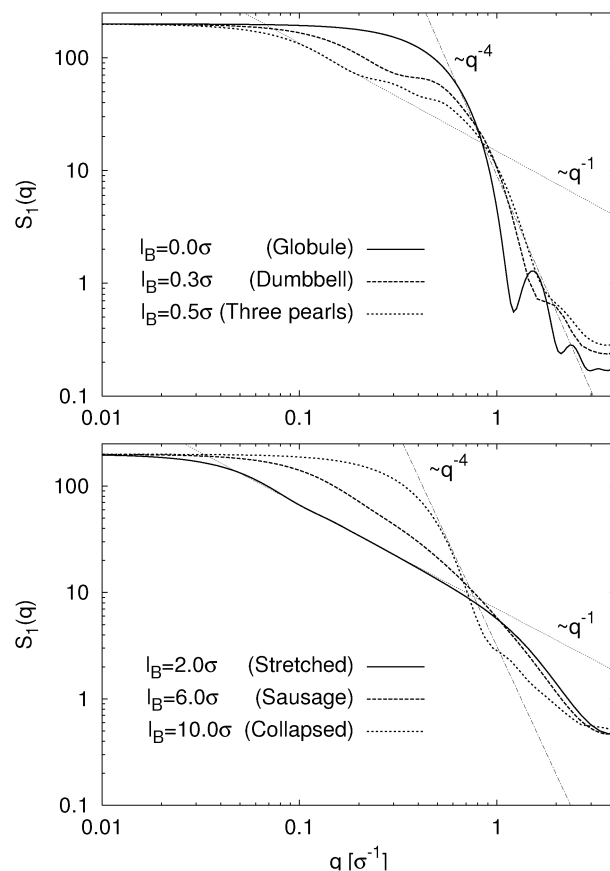


Figure 24. Form factors for the different conformation types while changing l_B for series C2. The straight lines indicate a stretched chain with $S_1 \propto q^{-1}$ and Porod scattering with $S_1 \propto q^{-4}$.

scale than the overall chain extension. The collapsed globule shows again, like the neutral globule, a strong decrease of the scattering intensity at large q -values. The rudimentary observable Porod scattering is strongly smeared out showing that the competition between attractive and repulsive forces induces large fluctuations on the surface of the globular object.

After this overview over the scattering of the different conformation types, we discuss the form factor of pearl-necklace conformations with a larger number of pearls in more detail. In this case, the scattering is not only influenced by the fluctuations in shape and size of the pearls and strings but also by the fluctuations of the structure type, namely, different numbers of pearls.

The form factor shows four different regimes, which resemble the different length scales that are involved in a pearl-necklace structure. For chains taken from series A1 with $N_m = 382$, the form factor is plotted in Figure 25. In the Guinier regime at $R_G q \ll 1$, the radius of gyration R_G can be calculated from $S_1(q) = N_m(1 - (R_G q)^2/3)$. This yields $R_G = 16.8\sigma \pm 0.3\sigma$ in good agreement with the directly calculated value $R_G = 16.9\sigma \pm 0.4\sigma$. In the range $0.07\sigma^{-1} \leq q \leq 0.4\sigma^{-1}$, the single-chain structure factor scales as $S_1(q) \propto q^{-1}$. The chain conformations are thus stretched on length scales larger than 15σ . At $q \approx 0.5\sigma^{-1}$, one can see a weakly pronounced shoulder in S_1 . A closer look to this region reveals that $S_1(q)$ has an inflection point at $q = 0.46\sigma^{-1}$, which is shown in Figure 26. A comparison with the intrapearl scattering shows that this is due to interpearl scattering. This becomes more clear when one looks at the analytic scattering function S_a of a linear arrangement of n homogeneous spheres with a diameter r_p and a distance r_{pp} . S_a is the product of the interpearl scattering S_{inter} and the

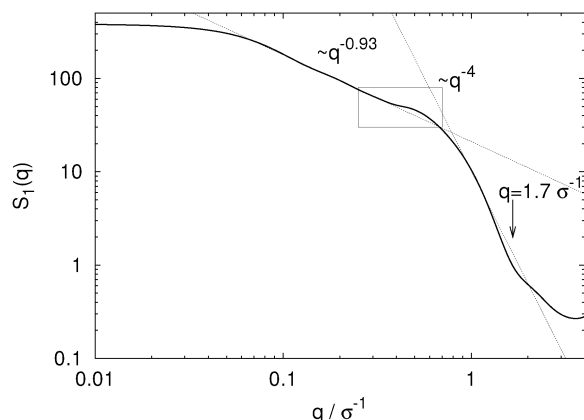


Figure 25. Form factor S_1 for typical pearl-necklace conformations. The dotted lines are fits to certain q -ranges, see text. The marked region is enlarged in Figure 26. The chains have a length $N_m = 382$ and on average $n_p = 4.5$ pearls.

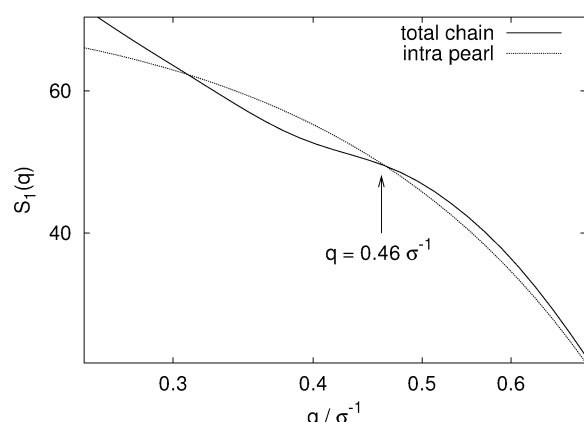


Figure 26. The pearl–pearl distance leaves only a very small signature in the form factor as can be seen in the close view of a comparison of the total form factor and the intrapearl form factor.

intrapearl scattering S_{intra} . The interpearl scattering is given by

$$S_{\text{inter}} = n + 2 \sum_{k=1}^{n-1} (n-k) \frac{\sin(qr_{\text{pp}}k)}{qr_{\text{pp}}k} \quad (16)$$

The intrapearl scattering is that of a homogeneous sphere and thus given by the Porod scattering:

$$S_{\text{intra}} = \frac{\sin(qr_p) - qr_p \cos(qr_p)}{qr_p^3} \quad (17)$$

Dividing out the intrapearl scattering from S_1 gives access to the interpearl scattering and thus r_{pp} . From the inflection point in the interpearl scattering, one can calculate the pearl–pearl distance. This yields $r_{\text{pp}} = 13.6\sigma$, again in accord with the directly measured value $r_{\text{pp}} = 13.3\sigma$. In the high q -range between $q \approx 0.9\sigma^{-1}$ and $q \approx 2.5\sigma^{-1}$, we find $S_1(q) \propto q^{-4}$, the typical Porod scattering with a small dip at $q \approx 1.7\sigma^{-1}$. Fitting the data to eq 17 yields a pearl radius $r_p \approx 2.6\sigma$, which again compares well to the directly calculated value $r_p \approx 3.0\sigma$.

We conclude that the cooperative effect of fluctuations on overlapping length scales broadens all characteristic signatures that can be revealed by scattering under experimental conditions such as polydispersity and line charge density fluctuations. Thus necklaces might be difficult to detect. We find the most pronounced necklace signatures for the dumbbell conformation.

9. Conclusion

We have studied a dilute solution of strongly charged polyelectrolytes in a poor solvent by means of molecular dynamics simulations for a variety of different parameters. We have developed a cluster algorithm to characterize pearl-necklace structures even for single configurations and performed an extensive data analysis of all of the pearl-necklace conformations in our simulations.

We found that the range in which scaling predictions are applicable is confined to a small range of parameters. One either has to stay close to the infinite dilution limit or use weakly charged chains to exclude counterion effects. The reason is that even in a dilute solution there is already a delicate interplay between the counterion distribution and the chain conformation for strongly charged chains. This became in particular evident in our investigations studying the dependence on the solvent quality and the Coulomb parameters ℓ_B and f .

Our results challenge approaches that apply Manning-like charge renormalization and simple scaling concepts to strongly charged polyelectrolytes. Because we found strong effects already for dilute solutions, we expect an even more complicated counterion chain coupling for semidilute and dense polyelectrolyte solutions.

We have discussed the different types of fluctuations present for pearl-necklace structures and quantified them for our data. We showed that the free energy differences between the structure types can be very small and that the size and position of the substructures exhibit large fluctuations.

In a preliminary classification of the phase space of PEs in poor solvent, we have shown that the phase space is multidimensional and that the region for pearl-necklace structures is rather small. In this context, we have also investigated the Coulomb-induced collapse of poor-solvent PEs, which appears to be a rather smooth transition. There, we have shown that the strong screening in the vicinity of the charged chains leads to sausage-like conformations instead of pearl necklaces. Our data suggest that the collapse is determined by the Bjerrum length because it occurs at $\ell_B \approx 8\sigma$ for all systems, which leads us to suggest that in the collapsed state ion–ion correlations proportional to ℓ_B play the most prominent part.

Finally, we computed some experimentally accessible observables such as the form factor and characteristic size ratios. This should help to analyze the experimental data and to discover pearl-necklace signatures which, according to our understanding, are not very pronounced.

Acknowledgment. We thank K. Kremer, B. Dünweg, B. Mergell, H. Schiessel, and M. N. Tamashiro for many fruitful discussions and comments. We also thank R. Everaers for contributions to the cluster algorithm. We gratefully acknowledge partial funding by the DFG SPP 1009 and SFB 625 and through the “Zentrum für Multifunktionelle Werkstoffe und Miniaturisierte Funktionseinheiten”, Grant BMBF 03N 6500.

Appendix A. Simulated Systems

Here, we give a detailed overview of the parameters of the simulated systems and some basic observables, namely, the chain length N_m , the end-to-end distance R_E , the hydrodynamic radius R_H , the characteristic ratios $r = (R_E/R_G)^2$ and $\alpha = R_G/R_H$, and the osmotic coefficient $\text{OC} = \Pi/p_{\text{ig}}$, where Π is the pressure and p_{ig} is the ideal gas pressure. If possible, also the number of pearls n_p and the average number of monomers in a pearl g_p is given. In the Tables 1–9, R_E , R_H , and ℓ_B are given in σ and ϵ in $k_B T$. All other quantities in the tables are

TABLE 1: Series A1^a

N_m	R_E	R_H	r	α	n_p	g_P	OC
48	3.48	2.19	3.25	0.88	1.00	46.0	0.96
94	4.56	2.71	3.40	0.91	1.01	93.9	0.68
142	12.9	4.11	4.63	1.46	1.97	68.8	0.60
190	15.0	4.60	4.49	1.54	2.01	90.4	0.44
238	25.7	5.86	5.84	1.83	2.94	75.5	0.46
286	30.4	6.51	6.10	1.89	3.24	82.5	0.42
334	38.2	7.44	6.73	1.98	3.94	78.6	0.40
382	45.4	8.24	7.24	2.05	4.53	78.0	0.35
430	55.4	9.22	7.55	2.19	5.22	75.2	0.36
478	59.7	9.81	7.61	2.20	5.60	78.3	0.39

^a $N_m = 48-478$; $\epsilon = 1.75k_B T$; $l_B = 1.5\sigma$; $f = 1/3$; $\rho_c = (1.0 \times 10^{-5})\sigma^{-3}$.

TABLE 2: Series A2^a

N_m	R_E	R_H	r	α	n_p	g_P	OC
99	26.8	5.59	7.17	1.79	2.77	23.3	0.54
199	68.1	10.43	8.20	2.28	4.13	20.7	0.32
299	102.9	14.37	8.88	2.40	5.99	18.9	0.39

^a $N_m = 100-300$; $\epsilon = 1.75k_B T$; $l_B = 1.5\sigma$; $f = 1/2$; $\rho_c = (6.7 \times 10^{-5})\sigma^{-3}$.

TABLE 3: Series A3^a

N_m	R_E	R_H	r	α	n_p	g_P	OC
99	22.1	5.08	6.72	1.68	2.89	25.1	0.46
199	54.9	9.15	8.24	2.09	5.25	21.4	0.36
299	83.4	12.6	8.69	2.24	7.68	20.4	0.35

^a $N_m = 100-300$; $\epsilon = 1.75k_B T$; $l_B = 1.5\sigma$; $f = 1/2$; $\rho_c = (6.7 \times 10^{-5})\sigma^{-3}$.

TABLE 4: Series B^a

ϵ	R_E	R_H	r	α	n_p	g_P	OC
0.00	102	16.2	8.88	2.11			0.66
0.50	100	14.9	9.28	2.21			0.62
1.00	82.2	13.1	8.81	2.11			0.63
1.25	68.7	11.0	8.44	2.15			0.53
1.35	58.5	9.78	7.91	2.13	5.70	25.2	0.52
1.45	45.9	8.22	7.32	2.07	5.12	35.6	0.53
1.55	34.3	6.89	6.56	1.94	3.92	52.9	0.45
1.65	24.2	5.83	5.76	1.73	2.91	76.8	0.48
1.75	16.8	5.03	4.72	1.54	2.14	108	0.36
1.85	13.8	4.68	4.36	1.41	1.90	123	0.31
2.00	11.2	4.34	4.21	1.26	1.52	155	0.26

^a $\epsilon = 0.0k_B T-2.0k_B T$; $N_m = 238$; $l_B = 1.5\sigma$; $f = 1/3$; $\rho_c = (5.0 \times 10^{-5})\sigma^{-3}$.

TABLE 5: Series C1^a

l_B	R_E	R_H	r	α	n_p	g_P	OC
0.0	4.41	3.27	2.22	0.91	1.0	200	0.97
0.083	15.8	4.70	4.04	1.67	2.0	95.3	0.94
0.25	72.1	10.6	7.99	2.41	3.83	21.1	0.86
0.5	111.3	14.9	9.51	2.42			0.75
0.75	124.8	16.3	9.88	2.44			0.63
1.0	129.5	17.0	9.98	2.41			0.55
1.25	125.8	17.1	9.70	2.36			0.46
1.5	130.2	17.1	10.2	2.39			0.40
3.0	104.8	15.9	9.34	2.16			0.18
6.0	67.66	13.0	8.22	1.82			0.06
8.0	31.94	8.46	6.74	1.45			0.06
10.0	9.204	5.45	3.04	0.97	1.0	200	0.04

^a $l_B = (0.0-12.0)\sigma$; $f = 1$; $\epsilon = 1.75k_B T$; $N_m = 200$; $\rho_c = (5.0 \times 10^{-5})\sigma^{-3}$.

TABLE 6: Series C2^a

l_B	R_E	R_H	r	α	n_p	g_P	OC
0.0	4.41	3.27	2.22	0.91	1.0	199	0.97
0.167	4.63	3.30	2.39	0.91	1.0	199	0.93
0.333	14.2	4.59	3.72	1.60	1.87	102	0.82
0.5	26.6	5.72	5.38	2.00	2.90	61.4	0.79
1.0	54.7	8.90	7.53	2.24	4.80	25.0	0.57
1.5	65.2	10.4	8.22	2.19			0.45
2.0	66.4	10.8	8.40	2.12			0.36
2.5	62.6	10.5	8.52	2.04			0.27
3.0	59.9	10.3	8.48	2.00			0.21
3.5	54.2	9.84	8.26	1.92			0.16
4.0	48.0	9.23	8.08	1.83			0.13
6.0	27.8	6.96	7.03	1.50			0.06
9.0	7.45	4.37	3.16	0.96	1.14	173	0.05

^a $l_B = (0.0-6.0)\sigma$; $f = 1/2$; $\epsilon = 1.75k_B T$; $N_m = 199$; $\rho_c = (5.0 \times 10^{-5})\sigma^{-3}$.

TABLE 7: Series C3^a

l_B	R_E	R_H	r	α	n_p	g_P	OC
0.0	4.41	3.27	2.22	0.91	1.0	199	0.97
0.25	4.59	3.29	2.37	0.91	1.0	199	0.93
0.5	5.10	3.31	2.86	0.91	1.0	199	0.76
0.75	10.5	4.04	4.01	1.30	1.62	120	0.64
1.0	13.0	4.39	4.24	1.44	1.87	104	0.54
1.25	13.5	4.51	4.22	1.46	1.98	97.4	0.47
1.5	13.5	4.50	4.38	1.43	1.95	99.2	0.38
2.25	12.2	4.47	4.32	1.31	1.57	125	0.29
3.0	12.3	4.44	4.90	1.25	1.30	152	0.22
4.5	9.86	4.29	3.99	1.25	1.06	188	0.10
6.0	7.77	4.06	3.39	1.04	1.01	198	0.15
9.0	6.35	3.82	3.07	0.95	1.00	199	0.07

^a $l_B = (0.0-9.0)\sigma$; $f = 1/3$; $\epsilon = 1.75k_B T$; $N_m = 199$; $\rho_c = (5.0 \times 10^{-5})\sigma^{-3}$.

TABLE 8: Series C4^a

l_B	R_E	R_H	r	α	n_p	g_P	OC
1.5	13.5	3.93	5.33	1.49	2.04	41.2	0.68
1.8	13.9	4.00	5.47	1.48	2.10	39.6	0.62
2.1	15.1	4.15	5.88	1.50	2.24	36.2	0.59
2.4	15.7	4.23	6.14	1.50	2.27	35.3	0.49
2.7	15.6	4.22	6.41	1.46	2.26	35.9	0.53
3.0	15.6	4.23	6.47	1.45	2.26	35.8	0.40
3.3	14.4	4.10	6.43	1.39	2.17	38.5	0.45
3.6	13.2	3.97	6.22	1.33	2.06	41.6	0.30
3.9	12.2	3.85	6.17	1.28	1.92	45.6	0.33
5.1	8.6	3.44	5.08	1.10	1.38	66.7	0.22
5.4	8.2	3.39	5.06	1.08	1.30	71.2	0.17
5.7	8.0	3.37	4.96	1.07	1.26	73.6	0.08
6.0	7.7	3.34	4.81	1.05	1.22	76.4	0.12
9.0	5.7	3.14	3.58	0.97	1.03	91.4	0.19
12.0	5.1	3.06	3.17	0.94	1.01	93.4	0.04

^a $l_B = (1.5-12.0)\sigma$; $f = 1/3$; $\epsilon = 1.5k_B T$; $N_m = 94$; $\rho_c = (1.0 \times 10^{-5})\sigma^{-3}$.

TABLE 9: Series D^a

l_B	f	R_E	R_H	r	α	n_p	g_P	OC
0.25	1.00	59.4	9.54	7.81	2.23	4.88	21.6	0.75
1.00	0.50	32.3	6.66	6.96	1.84	4.37	39.2	0.44
2.25	0.33	8.3	4.15	2.90	1.18	1.11	179	0.17
4.00	0.25	5.9	3.55	3.00	0.96	1.00	201	0.13

^a $l_B b^{-1} f^2 = 0.25 = \text{const}$; $\epsilon = 1.75k_B T$; $N_m = 200$; $\rho_c = (5.0 \times 10^{-4})\sigma^{-3}$.

dimensionless numbers. The statistical error for the chain extensions R_E and R_H is smaller than 10%. The parameter g_P exhibits a systematic error of plus or minus four monomers. For $g_P > 30$, the number of pearls has an accuracy of $\sim 5\%$.

For smaller g_p values, this error becomes larger. The statistical error of the pressure calculation gives rise to an error of the osmotic coefficient of ± 0.06 resulting in a large relative error for small values of OC.

References and Notes

- (1) Barrat, J.-L.; Joanny, J.-F. *Adv. Chem. Phys.* **1996**, *94*, 1–66.
- (2) Hara, M., Ed. *Polyelectrolytes: Science and Technology*; Marcel Dekker: New York, 1993.
- (3) Schmitz, K. S. *Macroions in solution and colloidal suspension*, 1st ed.; VCH Publishers: New York, 1993.
- (4) Förster, S.; Schmidt, M. *Adv. Polym. Sci.* **1995**, *120*, 51–133.
- (5) Holm, C.; Kékicheff, P.; Podgornik, R., Eds. *Electrostatic Effects in Soft Matter and Biophysics*; NATO Science Series II—Mathematics, Physics and Chemistry, Vol. 46; Kluwer Academic Publishers: Dordrecht, Netherlands, 2001.
- (6) Ghiggino, K. P.; Tan, K. L. In *Polymer photophysics*; Phillips, D., Ed.; Chapman and Hall: London, New York, 1985; Chapter 7, pp 341–375.
- (7) Kantor, Y.; Kardar, M.; Li, H. *Phys. Rev.* **1994**, *E49*, 1383.
- (8) Kantor, Y.; Kardar, M. *Phys. Rev. E* **1995**, *51*, 1299.
- (9) Dobrynin, A. V.; Rubinstein, M.; Obukhov, S. P. *Macromolecules* **1996**, *29* (8), 2974.
- (10) Schiessel, H.; Pincus, P. *Macromolecules* **1998**, *31*, 7953–7959.
- (11) Schiessel, H. *Macromolecules* **1999**, *32*, 5673–5680.
- (12) Dobrynin, A. V.; Rubinstein, M. *Macromolecules* **1999**, *32* (3), 915–922.
- (13) Dobrynin, A. V.; Rubinstein, M. *Macromolecules* **2001**, *34* (6), 1964–1972.
- (14) Solis, F. J.; de la Cruz, M. O. *Macromolecules* **1998**, *31* (16), 5502–5506.
- (15) Pickett, G. T.; Balazs, A. C. *Langmuir* **2001**, *17* (16), 5111–5117.
- (16) Migliorini, G.; Lee, N.; Rostiasvili, V.; Vilgis, T. A. *Eur. Phys. J. E* **2001**, *6* (3), 259–270.
- (17) Lyulin, A. V.; Dünweg, B.; Borisov, O. V.; Darinskii, A. A. *Macromolecules* **1999**, *32* (10), 3264–3278.
- (18) Chodanowski, P.; Stoll, S. *J. Chem. Phys.* **1999**, *111* (13), 6069–6081.
- (19) Micka, U.; Holm, C.; Kremer, K. *Langmuir* **1999**, *15*, 4033.
- (20) Micka, U.; Kremer, K. *Europhys. Lett.* **2000**, *49* (2), 189–195.
- (21) Limbach, H. J.; Holm, C. *J. Chem. Phys.* **2001**, *114* (21), 9674–9682.
- (22) Limbach, H. J.; Holm, C. *Comput. Phys. Commun.* **2002**, *147*, 321–324.
- (23) Holm, C.; Limbach, H. J.; Kremer, K. *J. Phys.: Condens. Matter* **2003**, *15*, S205–S211.
- (24) Limbach, H.; Holm, C.; Kremer, K. *Europhys. Lett.* **2002**, *60* (4), 566–572.
- (25) Spiteri, M. N.; Boue, F.; Lapp, A.; Cotton, J. P. *Physica B* **1997**, *234*, 303–305.
- (26) Carbajal-Tinoco, M. D.; Williams, C. E. *Europhys. Lett.* **2000**, *52* (3), 284–290.
- (27) Heinrich, M.; Rawiso, M.; Zilliox, J. G.; Lesieur, P.; Simon, J. P. *Eur. Phys. J. E* **2001**, *4* (2), 131–142.
- (28) Aseyev, V. O.; Klenin, S. I.; Tenhu, H.; Grillo, I.; Geissler, E. *Macromolecules* **2001**, *34* (11), 3706–3709.
- (29) Minko, S.; Kiriya, A.; Gorodyska, G.; Stamm, M. *J. Am. Chem. Soc.* **2002**, *124* (13), 3218–3219.
- (30) Lee, M.-J.; Green, M. M.; Mikes, F.; Morawetz, H. *Macromolecules* **2002**, *35* (10), 4216–4217.
- (31) de Gennes, P.; Pincus, P.; Velasco, R. *J. Phys.* **1976**, *37*, 1461.
- (32) Essafi, W.; Lafuma, F.; Williams, C. E. *J. Phys. II* **1995**, *5*, 1269–1275.
- (33) Heitz, C.; Rawiso, M.; François, J. *Polymer* **1999**, *40* (7), 1637–1650.
- (34) Waigh, T. A.; Ober, R.; Williams, C. E.; Galin, J.-C. *Macromolecules* **2001**, *34* (6), 1973–1980.
- (35) Baigl, D.; Williams, C. E. *Europhys. Lett.* **2003**, *62* (4), 588–594.
- (36) Limbach, H. J. *Struktur und Eigenschaften von Polyelektrolyten im schlechten Lösungsmittel*. Ph.D. Thesis, Johannes Gutenberg Universität, Mainz, Germany, 2001.
- (37) Deserno, M.; Holm, C. *J. Chem. Phys.* **1998**, *109*, 7678.
- (38) Deserno, M.; Holm, C. *J. Chem. Phys.* **1998**, *109*, 7694.
- (39) Grest, G. S.; Kremer, K. *Phys. Rev. A* **1986**, *33* (5), 3628–3631.
- (40) Liu, B.; Dünweg, B. *J. Chem. Phys.* **2003**, *118* (17), 8061–8072.
- (41) Schweins, R.; Huber, K. *Eur. Phys. J.* **2001**, *E5*, 117–126.
- (42) Belloni, L. *Colloids Surf.* **1998**, *A140*, 227.
- (43) Deserno, M.; Holm, C.; May, S. *Macromolecules* **2000**, *33*, 199–206.
- (44) Manning, G. *J. Chem. Phys.* **1969**, *51*, 924–933.
- (45) Oosawa, F. *Polyelectrolytes*; Marcel Dekker: New York, 1971.
- (46) Deserno, M. *Counterion condensation for rigid linear polyelectrolytes*. Ph.D. Thesis, Johannes Gutenberg Universität, Mainz, Germany, 2000.
- (47) Deserno, M.; Holm, C. In *Electrostatic effects in Soft Matter and Biophysics*; Holm, C., Kékicheff, P., Podgornik, R., Eds.; NATO Science Series II—Mathematics, Physics and Chemistry, Vol. 46; Kluwer Academic Publishers: Dordrecht, Netherlands, 2001.
- (48) Deshpandikar, A.; Obukhov, S.; Rubinstein, M. *Phys. Rev. Lett.* **2001**, *86* (11), 2341–2344.
- (49) Khokhlov, A. *J. Phys. A* **1980**, *13*, 979.
- (50) Vilgis, T. A.; Johner, A.; Joanny, J.-F. *Eur. Phys. J. E* **2000**, *2* (3), 289–300.
- (51) Deserno, M. *Eur. Phys. J. E* **2001**, *6*, 163–168.
- (52) Castelnovo, M.; Sens, P.; Joanny, J.-F. *Eur. Phys. J. E* **2000**, *1*, 115–125.
- (53) Stevens, M. J.; Kremer, K. *J. Chem. Phys.* **1995**, *103* (4), 1669–1690.
- (54) Winkler, R. G.; Gold, M.; Reineker, P. *Phys. Rev. Lett.* **1997**, *80*, 3731–3734.
- (55) Khan, M.; Jönsson, B. *Biopolymers* **1999**, *49*, 121.